Published by
NIGERIAN SOCIETY OF PHYSICAL SCIENCES
Available online @ https://journal.nsps.org.ng/index.php/jnsps

J. Nig. Soc. Phys. Sci. 4 (2022) 926

Journal of the Nigerian Society of Physical Sciences

A comparison of the performance and energy resolution of CdTe and Si detectors in the X-ray Fluorescence studies of metal samples and Alloys

Iniobong P. Etim[a,b,*], Rebecca Emmanuel Mfon[c]

[a] *Department of Physics, University of Surrey Guildford Surrey GU2 7XH, United Kingdom*
[b] *Department of Physics, University of Calabar, P.M.B 1115 Calabar, Cross River State, Nigeria*
[c] *Department of Physics Federal University of Lafia, P.M.B 146 Lafia, Nasarawa State, Nigeria*

Abstract

X-ray fluorescence provides a powerful means of non-destructively determining the elemental composition of a sample. X-rays from a Molybdenum (Mo) source was fired on copper, molybdenum, lead, steel and brass samples to determine their composition and relative abundance of their constituent elements. Two different detectors : the Cadmium Telluride (CdTe) and Silicon(Si) detectors were used to pick up the signals from the scattering of the X-rays at the sample surfaces and their energy resolutions as well as efficiencies were compared. With a non-noisy amplifier, the Si detector had a higher resolution (0.27 %) when compared to the 0.38 % for the CdTe detector but it had a lower efficiency when compared to that of the CdTe detector. It was also discovered that higher energies produced lower detector efficiencies.

DOI:10.46481/jnsps.2022.926

Keywords: X-ray fluorescence, Cadmium Telluride detector, Silicon detector, Energy resolution, energy efficiency

Article History:
Received: 09 July 2022
Received in revised form: 10 October 2022
Accepted for publication: 11 November 2022
Published: 27 November 2022

Communicated by: Edward Anand Emile

---

1. Introduction

X-ray fluorescence (XRF) is a technique which non-destructively analyses a material to identify the elements that make it up [1]. A material bombarded with high-energy X-rays absorbs it and emits characteristic secondary X-rays of lower energy but higher energy X-rays can also be produced using an X-ray tube [2]. Usually a heated cathode emits electrons, which are accelerated using an electric field to hit a metal target called an anode. When these electrons interact either with the orbit electrons of the atoms, they produce characteristic X-rays but when they interact with the nuclei of the target, they generate a continuum spectrum (bremsstrahlung radiation) [3].

The continuum spectrum can have energies between zero and the maximum energy of the incident electrons. The X-rays produced are then incident on a sample and if the incident photons have enough energy, they excite or ionize electrons of the inner orbits (photoelectric effect), producing a hole in the inner orbit and making the atom unstable. An electron from the outer orbits moves in to fill that hole resulting in the emission of a photon with energy equal to the energy difference of the initial and final states producing X-ray fluorescence (XRF) [4].

The energy of XRF is measured using a semiconductor de-

---

[*] Corresponding author tel. no: +234(0)8034451806
Email address: `ini2etim@unical.edu.ng` (Iniobong P. Etim)

tector. The signal from the detector is transferred to an amplifier and then to a multi-channel analyzer (MCA). The spectrum produced is visible and can be displayed on a computer screen. XRF is used for monitoring compliance with limits set by monitoring bodies [5] and for investigating soil samples to ascertain the extent of chemical weathering and possible vulnerability to gully erosion [6]. XRF is also used for forensic geoscience investigations and is a tool for environmental and criminal investigations [7]. XRF can be used to analyze elements in a material as the produced X-rays characterize each element and directly relates its amount in the material. That method is mainly used for metals, ceramics and glasses and apart from that, it is used in Archaeology and Geochemistry.

In this experiment, XRF produced from different metals and alloy samples are measured using two types of detectors. The characteristic X-ray peaks emanating from the samples aid the identification of the metals it contains and for alloys, the ratio of the different elements it contains was calculated. The energies of the characteristic X-rays from these samples were also calculated and obtained results were used to identify the metal/metals present in the investigated samples. The resolution and efficiencies of the two detectors as the angle the sample makes with the X-ray beam direction was changed to minimize self-absorption, were obtained and compared . The implication of all obtained results are discussed.

2. Background Theory

2.1. X-ray Fluorescence

The process of XRF is realized through the shell model of the atom. This model consists of a series of electron orbits (or shells) surrounding an atomic nucleus as shown in Figure 1. The proximity of a particular shell to the atomic nucleus reflects how tightly bound the electrons it houses are to that nucleus.

Thus the K-shell would then be the shell with the most tightly bound electrons. If an atom is excited from its ground state from an impinging photon via the photoelectric effect, the electrons would rearrange themselves to de-excite the atom resulting in the emission of a fluorescent X-ray photon [4].

To conserve momentum and energy, an incident photon is most likely to create a vacancy in the K-shell. Consequently, an electron from less bound shells (L, M etc) will be transferred to the vacancy emitting the fluorescent X-ray photon in the process with energy equal to the difference in binding energy between the two shells. The possible origins of a fluorescent X-ray are illustrated in Figure 2 [4]. Competing with XRF is the Auger process which dominates for lower atomic number (z) atoms. This is where the atom de-excites through the emission of an outer shell electron as opposed to an X-ray photon [4].

Mosely's law describes how the energy of the emitted fluorescent X-ray is proportional to Z^2 with a proportionality constant that depends on the shells involved in the emission as shown in Figure 2. (Z is the atomic number of an element) More specifically the relationship for the K and L line's X-ray frequency with Z is [8]:

$$K_\alpha : v_{x-ray} \sim (Z-1)^2 \quad (1)$$

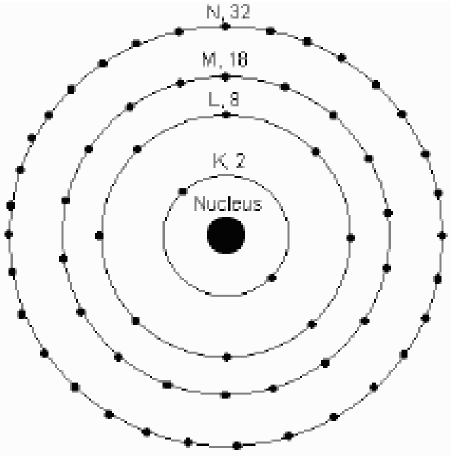

Figure 1. The Atomic shell structure. (http://earthsci.org/education/teacher/basicgeo/miner/electshells.gif)

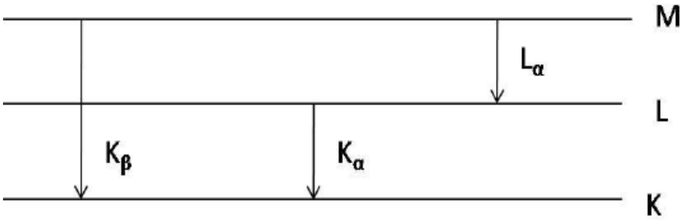

Figure 2. An illustration of possible sources of Fluorescent X-rays.

$$L_\alpha : v_{x-ray} \sim (Z-7.4)^2 \quad (2)$$

The additional constants of 1 and 4.5 account for the screening effect from outer shell electrons on the fluorescent X-ray. The XRF is considered a powerful tool for identifying elemental composition in materials because of the X-ray's energy strong dependence on the Z of its origin atom [8].

2.2. Self-absorption and Secondary emission

Self-absorption a frequent occurence in fluorescent X-ray spectroscopy is where X-rays produced from one atomic class in an alloy are absorbed by an atom of different atomic numbers. Fernandez *et al.* [9] further studied this phenomenon and sought for a means of correcting the intensity of X-rays for secondary emission. They suggested that the total intensity I_T of a characteristic line from an atom is a combination of XRF from the 'primary' excitation source, I_1 and the absorption of characteristic X-rays from other atoms which may then emit 'secondary' X-rays, I_2 [9]. Thus:

$$I_T = I_1 + I_2 \quad (3)$$

By considering the propagation plane of the incident and the fluoresced beam of photons as shown in Figure 3 the intensity of secondary emission dependence on the geometry can be appreciated. The effects of secondary emission can be removed by noting that $I_2 \rightarrow 0$ as the angle of the propagation plane $\alpha \rightarrow 90^o$.

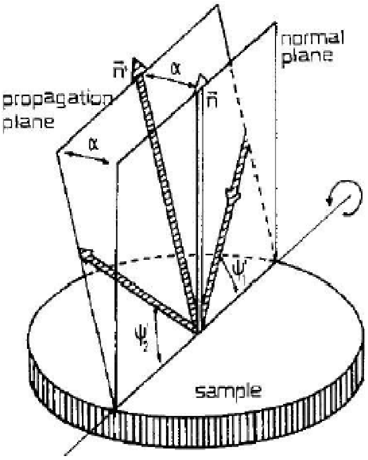

Figure 3. Propagation plane of incident and take off X-rays varied with α [9].

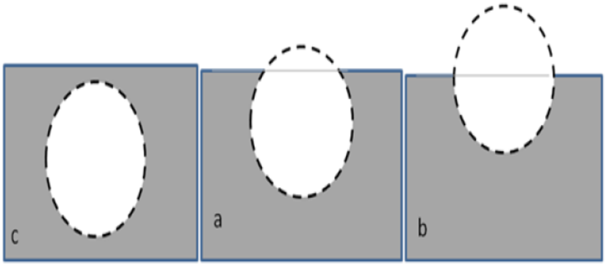

Figure 4. The I_2 probability bubble model for (c) $\alpha = 0^o$, (a) $0^o < \alpha < 90^o$ and (b) $\alpha = 90^o$ [9].

The mechanism of this process is described by a probability bubble by considering an infinitely long sample. Primary fluorescent X-ray photons are produced at the very center of the sphere and travel isotropically across the radius of the bubble and are absorbed producing a subsequent secondary emission at the surface of the sphere. When $\alpha = 0^o$ the position of the bubble is such that it is completely immersed in the material producing a large number of secondary photons which are emitted normal to the surface of the sample. Figure 4 shows that by increasing α, the probability bubbles begin to leave the material meaning that less secondary X-rays are produced.

Figure 5 shows the results of a Monte Carlo simulation (with 50,000 photons) published by Fernandez *et al.* [9] which shows the relationship between the Intensity of secondary photons as a function of angle α for a binary. Note how it falls to zero at 90^o as in accordance with the probability bubble model. Throughout this process, the intensity of the primary photons remains invariant to α, hence when $\alpha = 90^o$, $I_T = I_1$ [9].

2.3. Semiconductor Detectors

When a photon impinges on a semiconductor detector, electron-hole pairs are produced. Electrons move from the valence band to the conduction band and due to the electric field across the detector, they move to the positive electrode. A hole that is produced in the first position of the electron moves to the negative electrode. That charge created is measured across the detector.

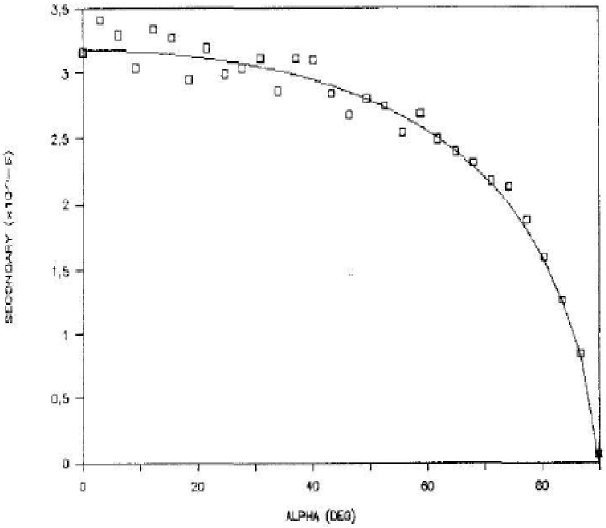

Figure 5. Secondary emission dependence on α from a Monte Carlo simulation developed in Pascal with 50,000 initial photons [9].

In this experiment, two different semiconductor detectors namely the Silicon (Si) and the Cadmium telluride (CdTe) detectors were used. In the Si detector, 3.6 eV is required to produce one electron-hole (e/h) pair while in the CdTe detector, 4.43 eV is required [4, 10].

In both Amptek detectors used, there is a high voltage across them to help in the collection of the charge and produce an increase in their efficiency. Conversely because that voltage is high, the resolution of the detector reduces and the effect from leakage current becomes more significant. That is why a thermoelectric cooler is installed just next to the detector and the pre-amplifier so that the electronic noise of the system is reduced and the resolution of the detector is enhanced as the peaks seem narrower. Apart from the cooler, there is a small monitor to read the temperature directly and the Beryllium window is used for the low energy photons (X-rays) [10]. At the range of low X-rays energies that were measured in this experiment, the Si detector resolution was compared to that of the CdTe detector. Thus the resolution of a peak given as a percentage is:

$$Resolution(\%) = \frac{FWHM}{Centroid} \times 100 \tag{4}$$

(where FWHM is the Full Width at Half Maximum of the peak and 'Centroid' is the centroid of the peak defined by the software).

At that chosen energy range, the CdTe detector has an extremely high efficiency. Thus to find the efficiency of the Si detector, which was assumed should be lower than that of the CdTe detector, the CdTe detector was assumed to be 100% efficient and the ratio of the two intensities gives the efficiency of the Si detector[10]. The error in resolution can be calculated using Equation 5 :

$$\sigma_R = R \cdot \sqrt{\left(\frac{\sigma_{FWHM}}{FWHM}\right)^2 + \left(\frac{\sigma_{Centroid}}{Centroid}\right)^2} \tag{5}$$

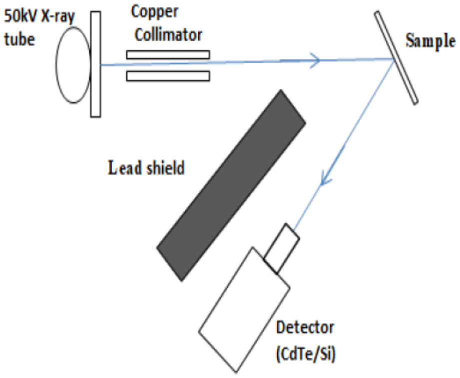

Figure 6. Experimental Setup showing the copper collimator, lead shield and Detector.

3. Methodology

3.1. Materials

An X-ray tube with an Air-cooled Mo K as a primary X-ray source was used. Si and CdTe detectors with gains 100 and 3 respectively were used. Other instruments included an Amplifier, a DP4 Digital pulse processor, a computer with software maestro which was used for data acquisition and samples studied were single element metals and Alloys in plate form.

3.2. System geometric setup/Calibration of CdTe detector

A copper sample was placed 30 *cm* from the X-ray source and the sample plate was turned at 45^o to the primary X-ray beam. The detector was placed at 45^o to the sample and 25 *cm* from it such that the angle between the X-ray beam and the detector axis is 90^o. In this setup, there was no beam collimator nor a shield between the collimator and the detector and so the detector energy calibration was done using Americium-241(241Am) .With the X-ray set at 50 *kV*, the sample was scanned for 500 *s* and a spectra was obtained. The spectra obtained had a large continuum background with no identifiable characteristic X-ray peaks and so another set up which was a modification of the first was created.

A copper collimator was placed in front of the X-ray source to bring to a focus on a limited area of the target, the primary X-ray beam and prevent them from spreading to hit the material around the system instead of the target. Furthermore, a lead shield was placed between the collimator and the detector to prevent the secondary X-rays from the collimator getting to the detector. The distance between the X-ray source and the sample was reduced to 20 *cm* while that between the sample and the detector was 10 *cm*. The angle between the primary X-ray beam and the detector axis was maintained at 45^o (Figure 6). With the X-ray source at 50 *kV* and for 500 *s*, another spectra of the calibration sample was obtained. The calibration plot is as shown in Figure 7.

The spectra for single-element samples like copper and lead as well as for alloys (brass and steel) were obtained and analysed.

The effects of secondary emission from the sample were also investigated using Si detector as illustrated in Figure 3. With the brass sample placed in the sample holder such that the incident X-ray beam was normal to the plane and with a brass collimator in place, the spectra for copper after 500 seconds was obtained. For X-rays of intensity 8.048 *keV*, the characteristic X-ray peak for copper was obtained. This process was repeated for various values of α ranging from 0^o to 90^o. Using the same setup but without a sample, the background was measured and obtained results are presented in Table 2.

Using the CdTe detector and the setup described above, the spectra of different samples were also collected in order to identify their composition from their characteristic X-ray peaks. Obtained results are presented in Table 2.

For the alloys, the ratio of their constituent elements was calculated by assuming that the amount of each element in the alloy sample is proportional to the number of counts in the peak of the characteristic lines of each element. The most abundant element was used as a reference to determine the abundance of the other constituent elements in the sample.

As was done with the CdTe detector, the spectra of the same samples were analysed with the Si detector to get each sample composition. The resolution of the Si detector was measured and obtained results were compared with those for the CdTe detector. The efficiency of the Si detector was also calculated and the ratio of the Si/CdTe intensities was measured and plotted as a function of the theoretical photon energy. The error for the ratio was calculated using:

$$\sigma_I = \sqrt{\left(\frac{\sigma_{I_{Si}}}{I_{CdTe}}\right)^2 + \left(\frac{I_{Si}\cdot\sigma_{I_{CdTe}}}{I^2_{CdTe}}\right)^2} \tag{6}$$

The uncertainties for the intensities, of Si and CdTe detectors:

$$\sigma_{I_{Si}} = \sigma_{I_{CdTe}} = \frac{\sigma N}{t} \tag{7}$$

The error of the number of counts was found from the Poisson statistics. The theoretical energy assumed that it does not have an error. Furthermore, for the Brass sample, the effect of varying the propagation plane angle α for the Cu 8.048 *keV* peak was also studied and the result is presented in Figure 12.

4. Results and Discussion

The calibration plot for the CdTe detector performed using the Am source is shown in Figure 7. A first-order polynomial fit is visible above using the equation $y = ax + b$, where $a = (0.017 \pm 0.003)\ keV$ and $b = (-0.061 \pm 0.006)\ keV$.

The values and errors for a and b were calculated from the software "OriginPro8" using the least-squares method. The error bars of the channel number are very small and therefore were not visible in the graph. The slope of the above plot gave the gain of the system as (0.017 ± 0.003) *keV*/*channel*.

The CdTe detector resolution was calculated using the spectrum for the calibration and Equation 4 and the error for each peak was calculated using Equation 5. Obtained results are as presented in Table 1.

The errors were very small so more decimal places were introduced and the CdTe detector resolution was high at 0.38 % with the poorest resolution being 3.37 %.

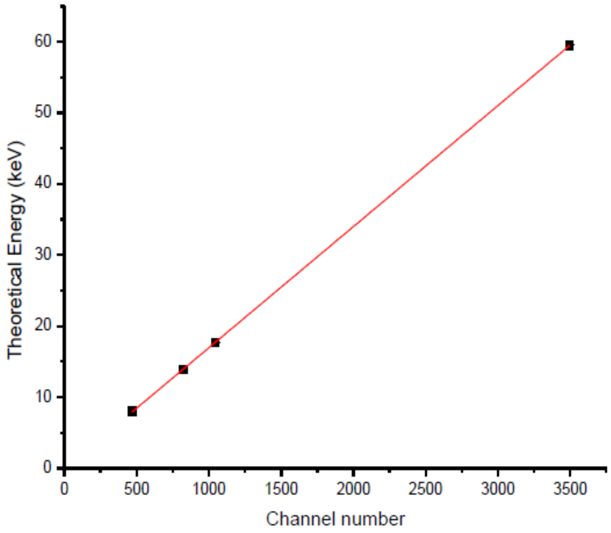

Figure 7. Theoretical Energy against the channel number (CdTe detector).

Table 1. Energy resolution of the CdTe detector.

Peak Energy (keV)	Energy Resolution (%)	Error in Resolution (%)
8.01	0.38	0.0001
13.90	3.37	0.0013
17.70	2.04	0.0005
59.50	0.99	0.0001

The energy of the characteristic X-rays of each sample was measured using the Maestro software which translated the obtained results to the peak centroid energy. The uncertainty for the energy was calculated using the standard error in the mean. The energies of the XRF of the samples in all cases except for lead were derived from the main peaks found in the spectra due to K_α characteristic line. K_α X-rays from lead have higher energies when compared with the range of energies measured ($\sim 79\ keV$), hence only L_α and L_β transition were seen in the spectrum and recorded in Table 2.

Table 2 shows the characteristic X-ray energies, the errors as well as the percentage differences between the obtained values and the published values for the other samples. The errors as in the first case are very small.

For lead, more than one transition was presented and the X-rays used were of high intensity and they were easily distinguished. The percentage difference was calculated using Equation 8 :

$$\%Difference = \left(\frac{Energy_{Theoretical} - Energy_{measured}}{Energy_{Theoretical}}\right) \times 100 \quad (8)$$

The background measurements show two peaks which are present in all spectra. The first peak at 16.61 keV is for the XRF produced from the X-ray tube. The X-ray tube is made of Mo and thus the visible peak in the spectrum has the energy of the $K\alpha$ X-ray of Mo. Furthermore, in all spectra, a peak with energy 7.80 keV was found. That peak is due to the XRF produced from the collimator which is made of Copper.

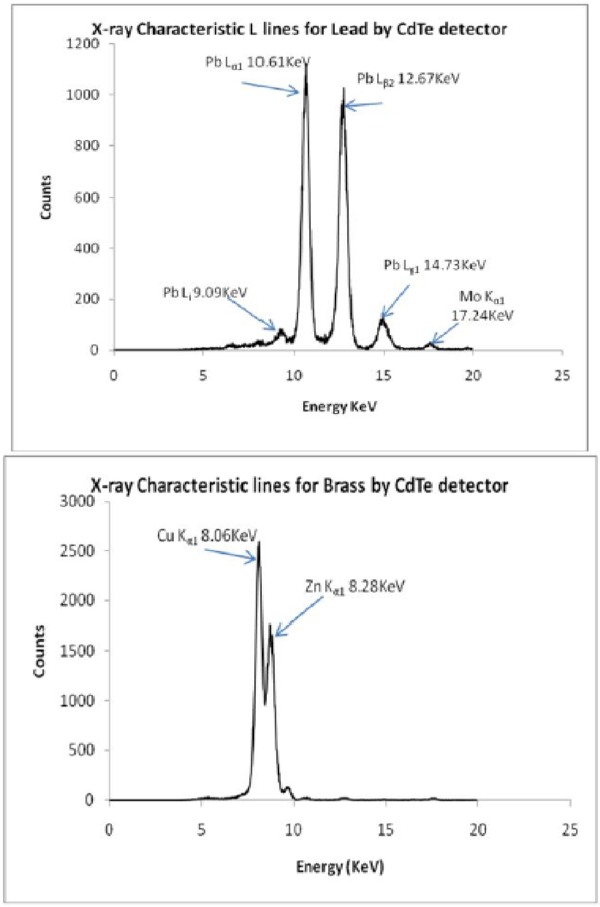

Figure 8. Spectra of characteristic X-rays of Lead and Brass.

Consequently, samples with a small amount of copper were not measured as the peak from copper was seen as a background peak. For the brass sample, the most abundant element is Copper. With this as the reference, the ratio of the counts for Zn peak to the counts of the Cu peak was calculated and found to be 1:0.25. By the same reasoning, for steel, the main element is iron (Fe) but Nikel(Ni) and Copper (Cu) are also available. Thus the ratio of Fe : Ni : Cu was found to be 1:0.20:0.03. The spectra showing the characteristic fluorescent X-rays for steel and Brass are shown in Figure 8.

4.1. Silicon (Si) detector calibration plot

The calibration plot for the Si detector is as shown in Figure 9. A first-order polynomial fit is visible above using the equation $y = ax + b$, where $a = (0.038 \pm 0.002)\ keV$ and $b = (-0.064 \pm 0.002)\ keV$.

The values and errors for a and b were calculated from the software "OriginPro8" using the least-squares method. The error bars of the channel number are very small and therefore not visible in the graph. The slope of the above plot gave the gain of the system which was $(0.038 \pm 0.002)\ keV/channel$. The energy resolution of the Si detector was measured and are as presented in Table 3.

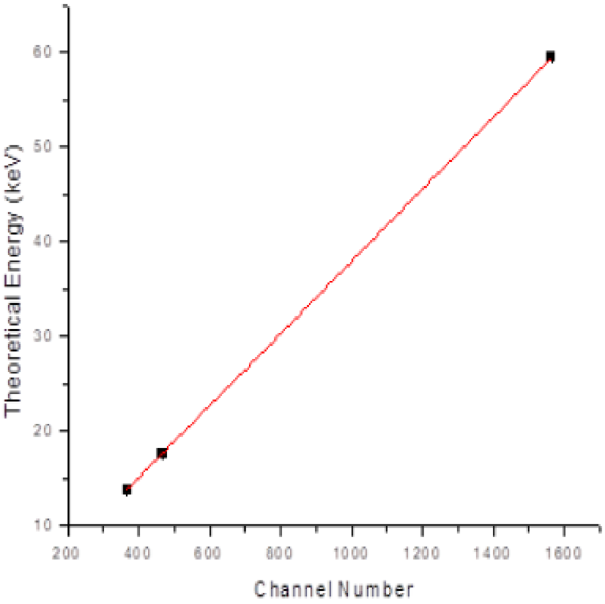

Figure 9. Calibration plot of the Silicon Detector.

Table 3. Energy resolution of the Si detector.

Peak Energy (keV)	Energy Resolution (%)	Error in Resolution (%)
13.90	4.29	0.0014
17.70	3.62	0.0010
59.50	0.27	0.0000

The errors for the Si detector as in the case of CdTe were very small so more decimal numbers were used in order to give a more accurate value.

The peaks measured from the background were the same peaks found when the CdTe detector was used. A comparison of the energy resolution of the Si detector (Table 3) with that of the CdTe detector (Table 1) shows that the resolution of the Si detector is lower. That was strange because at lower energy ranges, the Si detector has a higher resolution compared with the CdTe detector. This discrepancy was attributed to the noisy amplifier which may have reduced the resolution of the system. As before, the errors were very small so more decimal numbers were introduced.

The ratio of the elements in Brass, Cu:Zn was found to be 1:0.70. For the steel, as it is shown from Table 4, one peak was visible so the ratio of the different elements could not be calculated. This perhaps was due to the lower resolution of the Si detector using that amplifier. For a visible difference in the resolution of the Si detector, another amplifier was used (with shaping time equal to 12 μs). A new calibration plot (Figure 10) was done for the Si detector with the new amplifier and the obtained results were found to be completely different.

A first-order polynomial fit is visible above using the equation $y = ax + b$, where $a = (0.014 \pm 0.003)$ keV and $b = (0.014 \pm 0.001)$ keV. The values and errors for a and b were calculated as above. The error bars of the channel number are very small and therefore cannot be visible in the graph. The slope of the above chart gives the gain of the system. Therefore, it can be seen that the gain is equal to (0.014 ± 0.003) $keV/channel$. The resolution was then calculated and compared with the previous one (Table 5).

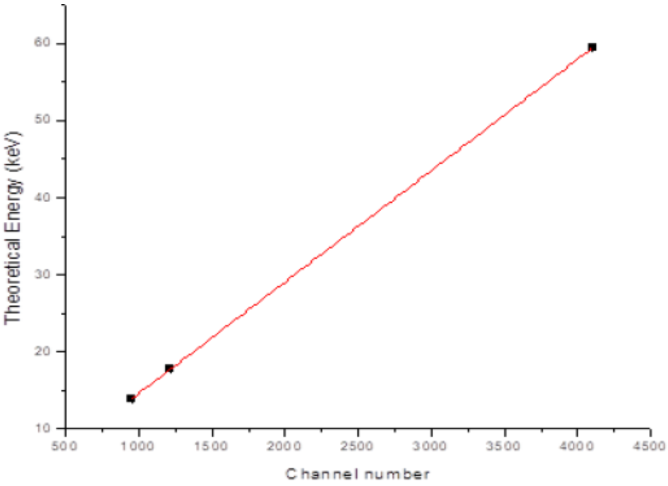

Figure 10. New calibration plot for Si detector used with new amplifier.

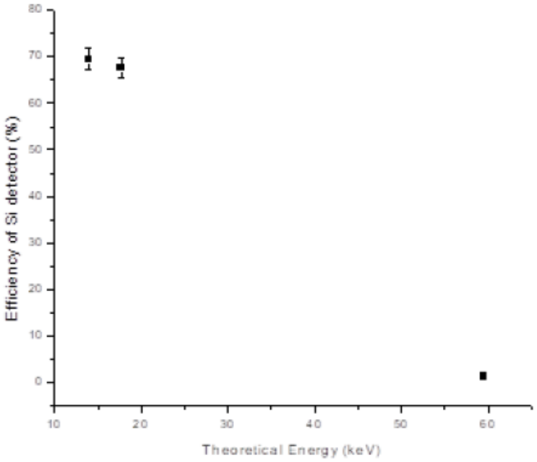

Figure 11. Silicon detector efficiency relative to CdTe detector.

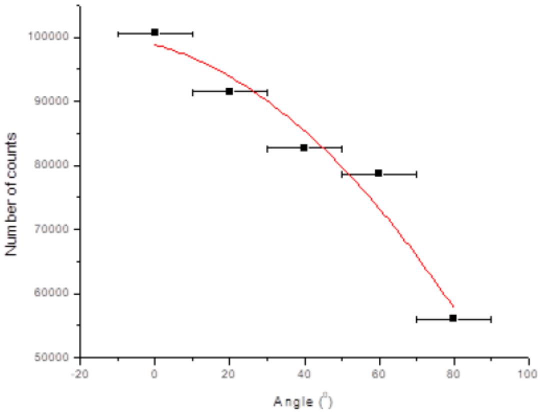

Figure 12. Total Intensity dependence on α for a Cu 8.048 keV peak.

Table 4. Showing the sample composition and identified elements with their characteristic X-ray energies and associated uncertainties for Si detector

Sample	Element	Characteristic X-ray energy (keV)	Uncertainty of the X-ray Energy (keV)	Published X-ray Energy (keV)	Percentage difference
Background	Mo	16.41	0.00319	17.479	6.116
	Cu	7.44	0.00681	8.048	7.555
Copper	Cu	8.00	0.00009	8.048	0.596
Mo	Mo	17.33	0.00029	17.479	0.852
Lead	Pb	14.73	0.00093	14.765	0.237
	Pb	12.53	0.00026	12.614	0.666
	Pb	10.48	0.00067	10.551	0.673
Brass	Cu	7.96	0.00014	8.048	1.093
	Zn	8.57	0.00013	8.639	0.799
Steel	Fe	8.53	0.00012	6.404	33.198
	Ni	8.53	0.00012	7.478	14.068
	Cu	8.53	0.00012	8.048	5.989

Table 5. New energy resolution for Si detector with new amplifier

Peak Energy (keV)	Energy Resolution (%)	Error in Resolution (%)	New Resolution (%)	Error in New Resolution (%)
13.90	4.29	0.0014	2.13	0.0005
17.70	3.62	0.0010	1.65	0.0004
59.50	0.27	0.0001	0.04	0.0001

Table 6. Showing the new sample composition for Brass and Steel with their characteristic X-ray energies and associated uncertainties for Si detector with new amplifier

Sample	Element	Characteristic X-ray energy (keV)	Uncertainty of the X-ray Energy (keV)	Published X-ray Energy (keV)	Percentage difference
Brass	Cu	6.29	0.00066	6.404	1.780
	Zn	8.61	0.00037	8.048	6.983
	Fe	8.00	0.00037	6.404	1.780
Steel	Cu	7.98	0.00464	8.048	0.845
	Ni	7.01	0.00084	7.478	6.258
	Fe	6.36	0.00032	6.404	0.687

With the new amplifier, a higher resolution of the Si detector was obtained from the new spectra produced. For the errors as before were very small and so more decimal numbers were used in order to give a more accurate. To test how efficient the Si detector was with new amplifier, the spectra for brass and steel were acquired and the results are displayed in Table 6. The errors were small and the peaks were easily distinguished. The ratios of the constituent elements in these two Alloys were calculated and for Brass, a peak due to iron (Fe) though of a lower intensity could be distinguished because now the detector resolution was higher (recall that with the CdTe detector that peak was not visible). The ratio Cu:Zn:Fe in Brass was found to be 1:0.53:0.01 while the ratio Fe:Ni:Cu for Steel was 1:0.14:0.01.

The efficiency of the CdTe detector was assumed to be 100% and thus the ratio of the intensities gives the efficiency of the Si detector and high energies were found to produce lower detector efficiencies. This is because photons with higher energies move faster in the detector and intereact less with the sample so the number of counts measured is less and resulted in a lower efficiency.

The graph which shows the total number of counts from fluorescent X-rays in the 8.048 *keV* Cu characteristic X-ray peak of the brass sample for different inclination angles α shows that the intensity decreases as α increases suggesting a reduction in the enhancement from self-absorption and secondary X-ray emission as predicted by Fernandez's bubble model.

For this data to correctly fit the model, the photons from the X-ray tube have to be heavily collimated to produce a thin beam. The Monte Carlo simulation results in Figure 5 was produced from modeling a point beam but the same level of collimation could not be achieved experimentally as the risk of no XRF hitting the detector at all and also the scattering continuum would dwarf any characteristic X-ray peaks present. Moreover, the model assumes an infinitely long and thick sample, although due to the probabilistic nature of photon, not all the X-rays will be absorbed, and the sample thickness will have a direct consequence on the number of counts.

5. Conclusion

This project developed a means of non-destructively determining the composition of metals through a study of the energy of their emitted characteristic X-rays. A Mo source X-ray tube collimated to scatter off a sample at a 45^o incidence and take-off angle to a semiconductor detector was used. The intensity of the characteristic X-ray energy peaks from different samples was used for estimating the abundance of particular elements in each sample.

The silicon detector superior resolution over that of the CdTe detector proved to be a much better tool for correctly identifying energy peaks. However, its reduced efficiency translated to poor counting statistics at higher energies as seen from the reduced energy resolution for a $^{241}Am\ \gamma - peak$ at 59.5 keV for the silicon detector. Thus higher energies were found to produce lower detector efficiencies.

The peak intensities from steel and brass alloys were used to estimate element composition and these produced reasonable abundances of zinc compared to copper. The investigation into the correction of secondary emission was done using the ‘probability bubble’ model described by Fernandez *et al.* [9]. Experimentally the dependence on total intensity on the angle α compares well with the model. The limiting factors in this technique however lie in the level of collimation that can be placed on the beam without reducing counting statistics to an unacceptable level and preventing the scattering component from dwarfing any characteristic lines present. To extend this study, it might be necessary to develop a setup that can measure the angle α much more accurately.

Acknowledgments

We thank the referees for the positive enlightening comments and suggestions, which have greatly helped us in making improvements to this paper. The authors would also like to thank Dr. Annika Lohstroh, Prof. Paul Sellin, Gary Strudwick and John-William Brown of the Department of Physics University of Surrey for their guidance and technical assistance.

References

[1] H. Ait Bouh, “*X-ray fluorescence analysis techniques:Principles and instrumentations*”, LAP Lambert Academic Publishing (2020) ISBN 978-620-2-78771-0.

[2] P. Mudgal, D.J. Bell, “X-ray production/Radiology Reference article/”, Radiopaedia.org, https://doi.org/10.53347/rID-25428.

[3] G. Lloyd-Jones, “Basics of X-ray Physics-X-ray production”, https://www.radiologymasterclass.co.uk/tutorials/physics.

[4] G. F. Knoll, “*Radiation Detection and Measurement*”, Wiley Publishers, 4th Edition, (2010) ISBN 978-0-470-13148-0.

[5] M. Alghamdi , M A-E. Abdallah, S. Harrad, “The utility of X-Ray fluorescence spectrometry as a tool for monitoring compliance with limits on concentrations of halogenated flame retardants in waste polymers: A critical review”, Emerging contaminants **8** (2022) 9, https://doi.org/10.1016/j.emcon.2021.12.002.

[6] D. J. Kalnicky, R. Singhvi, “Field portable XRF analysis of environmental samples”, Journal of hazardous materials **83** (2001) 93, https://doi.org/10.1016/s0304-3894(00)00330-7.PMID:11267748.

[7] F. L. Melquiades, C. Appoloni, “Application of XRF and field portable XRF for environmental analysis”, Journal of Radioanalytical and Nuclear Chemistry **262** (2004) 533, https://doi.org/10.1023/B:JRNC.0000046792.52385.b2.

[8] H. K. Herglotz & L. S. Birks, “*X-ray Spectrometry*”, ISBN 0-8247-6625-3, New York.

[9] J. E. Fernandez, “Monte Carlo computer simulation of the XRF intensity dependence on the propagation plane inclination”, Computer Physics Communications (1989): 54211, https://doi.org/10.1016/0010-4655(89)90083-0.

[10] Laboratory Script: RDI23-Si and CdTe X-ray Spectroscopy, Professor Paul Sellin (2009).